The *Similar Seven*: A Set of Very Alike Exoplanets to Test Correlations between System Parameters and Atmospheric Properties

Chima D. McGruder[1,5] , Mercedes López-Morales[1] , Rafael Brahm[2,3,4] , and Andrés Jordán[2,3,4]

[1] Center for Astrophysics | Harvard & Smithsonian, 60 Garden St, Cambridge, MA 02138, USA; chima.mcgruder@cfa.harvard.edu
[2] Facultad de Ingeniería y Ciencias, Universidad Adolfo Ibáñez, Av. Diagonal las Torres 2640, Peñalolén, Santiago, Chile
[3] Millennium Institute for Astrophysics, Santiago, Chile
[4] Data Observatory Foundation, Chile

Abstract

Studies of exoplanetary atmospheres have found no definite correlations between observed high-altitude aerosols and other system parameters. This could be, in part, because of the lack of homogeneous exoplanet samples for which specific parameters can be isolated and inspected. Here, we present a set of seven exoplanets with very similar system parameters. We analyze existing photometric time series, Gaia parallax, and high-resolution spectroscopic data to produce a new set of homogeneous stellar, planetary, and orbital parameters for these systems. With this, we confirm that most measured parameters for all systems are very similar, except for the host stars' metallicities and possibly high-energy irradiation levels, which require UV and X-ray observations to constrain. From the sample, WASP-6b, WASP-96b, and WASP-110b have observed transmission spectra that we use to estimate their aerosol coverage levels using the Na I doublet 5892.9 Å. We find a tentative correlation between the metallicity of the host stars and the planetary aerosol levels. The trend we find with stellar metallicity can be tested by observing transmission spectra of the remaining planets in the sample. Based on our prediction, WASP-25b and WASP-55b should have higher levels of aerosols than WASP-124b and HATS-29b. Finally, we highlight how targeted surveys of alike planets similar to the ones presented here might prove key for identifying driving factors for atmospheric properties of exoplanets in the future and could be used as a sample selection criterion for future observations with, e.g., JWST, ARIEL, and the next generation of ground-based telescopes.

Unified Astronomy Thesaurus concepts: Atmospheric clouds (2180); Exoplanet atmospheres (487); Exoplanet atmospheric composition (2021); Ephemerides (464)

1. Introduction

The upper atmospheres of about 100 exoplanets have been probed via transmission spectroscopy to date with HST, Spitzer, ground-based telescopes (NASA Exoplanet Science Institute 2019),[6] and now JWST (JWST Transiting Exoplanet Community ERS team et al. 2022). Most observations suggest that atmospheric features are heavily muted by aerosols (e.g., Wakeford et al. 2019), with only a few planets showing little to no aerosol coverage (e.g., Kirk et al. 2019; Alam et al. 2021; Ahrer et al. 2022; McGruder et al. 2022).

The formation of aerosols in planetary atmospheres occurs via complex chemical and physical processes, which are not yet fully understood, but work is in progress (see, e.g., Helling 2008; Marley et al. 2013; Helling 2019; Gao et al. 2021). For example, predictions link cloud formation in exoplanets to the chemical composition of their atmospheres, where *seed* particles need to be lofted to high altitudes so gases can condense on them and form clouds (e.g., Helling 2008, and references therein). The composition, availability, and altitude of potential *seed* particles has many dependencies, including the composition of the protoplanetary disk (e.g., Mordasini et al. 2010), and atmospheric differentiation, where heavier

elements are expected to sink into the lower layers of the atmosphere (e.g., Helling 2019). In the case of hazes, model predictions show that high-altitude hazes can form in exoplanets via UV-driven photolysis (e.g., Moses et al. 2011, 2013), and laboratory experiments have shown that UV radiation can form photochemical hazes in H_2-dominated atmospheres at temperatures between 600 and 1500 K (Fleury et al. 2019).

Understanding what system parameters drive the presence or absence of aerosols in exoplanetary atmospheres will be key to understanding their formation and evolution mechanisms. However, comparative studies of exoplanet atmospheres so far have yielded either no correlations between the atmospheric properties of the planets studied and other system parameters (see, e.g., Sing et al. 2016), or only tentative correlations between planetary equilibrium temperature and atmospheric aerosol levels (Heng 2016; Stevenson 2016; Fu et al. 2017; Tsiaras et al. 2018; Dymont et al. 2022). Yet degeneracies between system parameters and disagreeing observations leave any correlation uncertain (Alam et al. 2020).

Possible reasons for why correlations between observed exoplanet atmospheric properties and other system parameters have not yet been found are the fact that the parameter space being considered is too broad, with multiple independent parameters typically being fitted simultaneously (e.g., planetary equilibrium temperature, density, log surface gravity, planetary/host star metallicity, etc.) and over wide ranges of values, as well as the parameter space being scarcely sampled, with typically one-to-no pairs of similar planets being examined.

---

[5] NSF Graduate Research Fellow.

[6] Accessed on 2022 May 29.

We present a way to potentially alleviate this problem by identifying groups of planets with similar properties, so that a reduced number of parameters can be isolated and compared against observed atmospheric features of the planets in detail. In particular, we have identified a group of seven gas giants with very similar parameters, except for the metallicity of their host stars and possibly their high-energy irradiation levels. We use this group of planets to test whether aerosol properties are related to those parameters.

Section 2 describes the identification of the sample. Sections 3 and 4 present our reanalysis of system parameters and observed transmission spectra for comparative purposes. Section 5 presents the analysis of correlations between exoplanet aerosol level proxies and the host star metallicity and high-energy irradiation levels. Finally, Section 6 summarizes our results.

2. The Sample

Using the NASA Exoplanet Archive (NASA Exoplanet Science Institute 2021),[7] we compiled system parameters for all known exoplanets with an observed optical or near-infrared transmission spectrum. We compiled the planets' mass, radius, orbital period, and semimajor axis separation, as well as the mass, radius, effective temperature, and metallicity of the host stars. With those values in hand, we computed the planets' gravity, density, equilibrium temperature, and their stellar insolation levels in Earth units. We then searched in the compiled list for planets with very similar system parameters and compared their observed transmission spectra.

This is how we identified WASP-6b and WASP-96b, two hot Jupiters with very similar masses, radii, T_{eq}, stellar parameters, and insolation levels (see top six panels of Figure 1 and Table 1), but strikingly different transmission spectra (see bottom three panels of Figure 1 and Section 4). From the parameters available for each system, they only appear to differ significantly in the host star metallicity, reported in the NExSci database as $[Fe/H] = -0.20 \pm 0.09$ for WASP-6b (Gillon et al. 2009), and $[Fe/H] = 0.14 \pm 0.19$ for WASP-96b (Hellier et al. 2014).

Next, we compared the parameters of all known exoplanets, including those without atmospheric observations, to those of WASP-6b and WASP-96b, assuming the planets to be similar if all their planetary parameters listed above agreed within about 1σ. Using this strategy, we found another five planets *similar* to WASP-6b and WASP-96b: WASP-25b (Enoch et al. 2011), WASP-55b (Hellier et al. 2012), WASP-110b (Anderson et al. 2014), WASP-124b (Maxted et al. 2016), and HATS-29b (Espinoza et al. 2016). This is how we arrived to the *similar seven* planets sample described in the remaining of the paper. The parameters of each system, rederived homogeneously as described in the following section, are summarized in Table 1.

3. Derivation of Homogeneous Star and Planet Parameters

The parameters used in Section 2 to identify the sample were obtained from various literature sources. Therefore, to minimize potential biases and systematics between separate analyses, we rederived the parameters of each system homogeneously. Table 1 provides all the newly derived

parameters, with the derivation processes of each set of parameters described below.

3.1. Stellar Parameters

We rederived the stellar parameters of each host star using archival HARPS (Mayor et al. 2003) and FEROS (Stahl et al. 1999) spectra.[8] Each spectrum was homogeneously reduced using CERES (Brahm et al. 2017a), and the stellar parameters (T_{eff}, log g, [Fe/H], $v \sin I$) were derived using ZASPE (Brahm et al. 2017b), as described in detail in Brahm et al. (2019, 2020). Once ZASPE had obtained the stellar atmospheric parameters, the remaining physical parameters were computed comparing synthetic values generated using PARSEC isochrones (Bressan et al. 2012) and Gaia DR2 (Gaia Collaboration et al. 2018) parallaxes. For this step, we fixed the stellar metallicity to the values obtained by ZASPE and used T_{eff} from ZASPE as a prior to obtain posterior distributions for the stellar age, mass, and interstellar extinction using emcee (Foreman-Mackey et al. 2013). From these values, we also derived stellar radii and log g, which was then fed back into ZASPE as a fixed parameter. The process described above was iterated until reaching convergence in log g. For WASP-55, which has both HARPS and FEROS observations, we weighted averaged the values from each instrument.

3.1.1. R'_{HK} Activity Index

We derived R'_{HK} values for each host star from the Ca II H&K lines in their HARPS and FEROS spectra, following the methods in Noyes et al. (1984), and calibrated them to the standard Mount Wilson scale following Lovis et al. (2011). To calibrate the R'_{HK} indexes from HARPS and FEROS to the Mount Wilson scale, we used six of the seven (all but HD 219834) reference stars used by Lovis et al. (2011) that have both HARPS and FEROS spectra. For HARPS, we found a conversion of the form $S_{MW} = 1.118 \cdot S_{HARPS} + 0.0135$, with a 0.0035 fit dispersion. For FEROS, we found the conversion $S_{MW} = 1.2121 \cdot S_{FEROS} + 0.0072$, with a 0.0275 fit dispersion.

3.1.2. Rotational Period

We estimated the rotation period, P_{rot}, of each star using three proxies: (1) $v \sin I$ from Section 3.1, using the equation

$$P_{rot} = 2\pi R_*/v \sin(i - \lambda), \qquad (1)$$

where R_* is the stellar radius, i is the inclination of the planet's orbital axis, and λ is the rotation axis alignments, where the value of λ has been measured for WASP-6 and WASP-25 (Gillon et al. 2009; Brown et al. 2012; Tregloan-Reed et al. 2015) and we estimated it for the remaining stars using probability distributions (see Appendix A); (2) TESS (Ricker et al. 2014) and ASAS-SN (Shappee et al. 2014; Kochanek et al. 2017) light curves (see Appendix B); and (3) the R'_{HK} indexes derived above, combined with Table 3 and Equation (6) of Suárez Mascareño et al. (2016).

The values of P_{rot} obtained via each method are summarized in Table 1. The values obtained with the first two methods are consistent with each other, while the values obtained using R'_{HK} are not fully consistent. Because the periods obtained from the first two methods are more direct measurements, we

---

[7] Accessed on 2021 November 17.
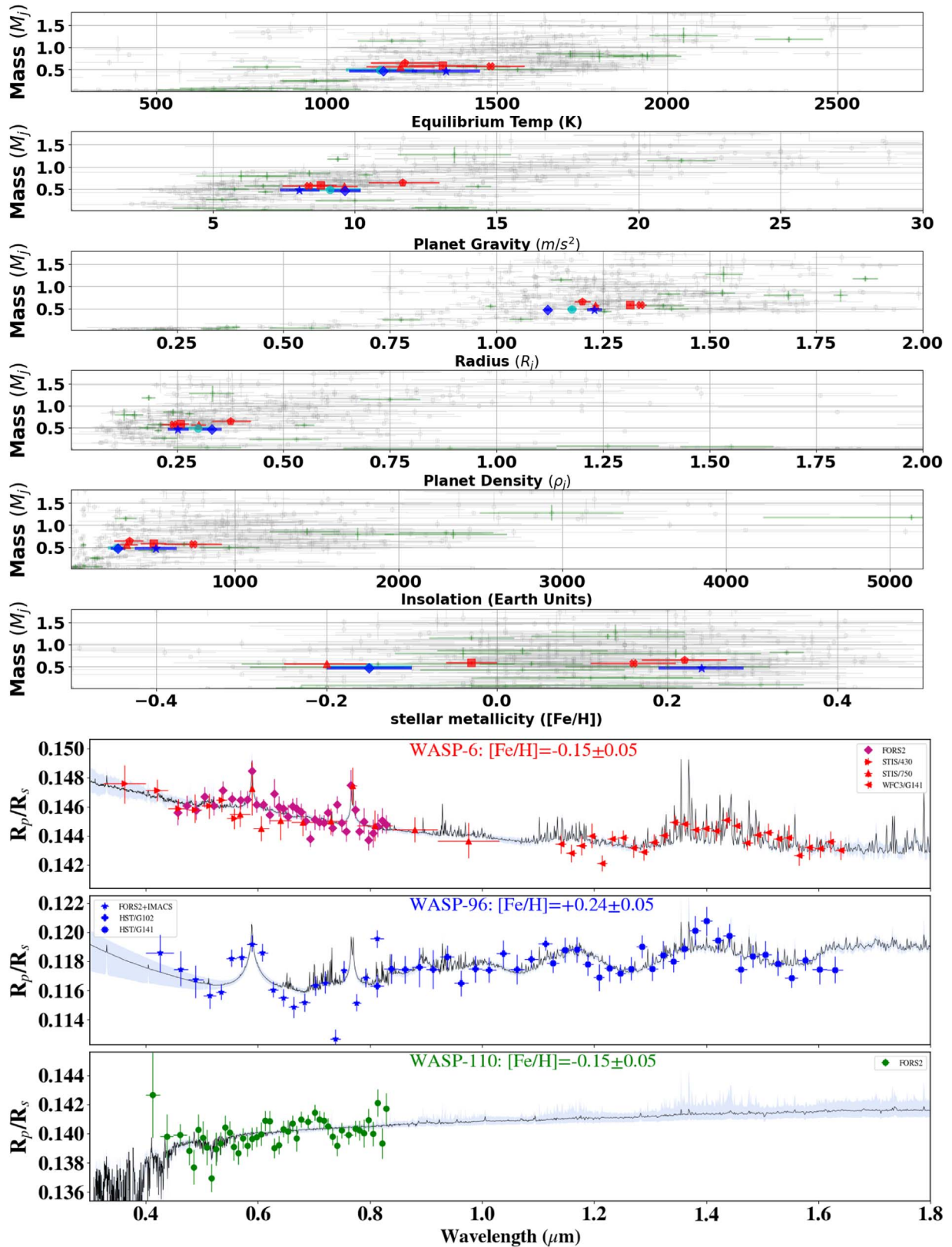
[8] archive.eso.org

Figure 1. Top: Mass vs. equilibrium temperature, gravity, radius, density, stellar irradiation, and star's metallicity for WASP-6b (blue diamonds), WASP-96b (blue stars), WASP-110b (cyan circles), WASP-124b (red "X"), WASP-55b (red squares), WASP-25b (red triangle), HATS-29b (red pentagon), the PanCET planets (green crosses), and all exoplanets with measured parameters (gray circles). The Equilibrium Temperature, Insolation, and metallicity of WASP-110b and WASP-6b overlap (see Table 1), making it hard to see the cyan circles of WASP-110b underneath the blue diamonds of WASP-6b. Bottom: Transmission spectrum of WASP-6b (red/magenta, Nikolov et al. 2015; Carter et al. 2020), WASP-96b (blue, Nikolov et al. 2018; Yip et al. 2021; Nikolov et al. 2022; McGruder et al. 2022), and WASP-110b (green circles, Nikolov et al. 2021), with the Platon best-fit retrieval model (black line) and 1σ confidence interval (cyan shaded regions) overplotted. In this figure, the parameters for the *similar seven* planets are the rederived parameters discussed in Section 3.

Table 1
Stellar and Planetary Parameters of All Similar Seven Systems

Param.	WASP-6	WASP-25	WASP-55	WASP-96	WASP-110	WASP-124	HATS-29
M_*	$0.854^{+0.027}_{-0.023}$	$0.962^{+0.027}_{\pm0.021}$	1.071 ± 0.025	$1.03^{+0.031}_{-0.036}$	$0.814^{+0.014}_{-0.022}$	$1.157^{+0.016}_{-0.015}$	$1.055^{+0.036}_{-0.038}$
R_*	$0.79^{+0.008}_{-0.009}$	$0.884^{+0.008}_{-0.009}$	$1.09^{+0.012}_{-0.013}$	$1.055^{+0.018}_{-0.017}$	0.853 ± 0.011	$1.074^{+0.013}_{-0.015}$	$1.066^{+0.018}_{-0.019}$
$T_{\rm eff}$	5438 ± 50	5697 ± 80	6096 ± 71	5678 ± 80	5392 ± 50	6258 ± 100	5769 ± 80
$\log_{10}(G_*)$	$4.565^{+0.022}_{-0.016}$	$4.529^{+0.018}_{\pm0.014}$	4.393 ± 0.015	$4.404^{+0.023}_{-0.026}$	$4.487^{+0.013}_{-0.018}$	$4.439^{+0.01}_{-0.009}$	4.406 ± 0.024
ρ_*	$1.73^{+0.08}_{-0.07}$	$1.391^{+0.058}_{-0.048}$	$0.822^{+0.036}_{-0.035}$	$0.876^{+0.05}_{-0.054}$	$1.31^{+0.055}_{-0.062}$	$0.933^{+0.041}_{-0.036}$	$0.869^{+0.055}_{-0.054}$
[Fe/H]	-0.15 ± 0.05	-0.2 ± 0.05	-0.03 ± 0.04	0.24 ± 0.05	-0.15 ± 0.05	0.16 ± 0.05	0.22 ± 0.05
$v \sin I$	1.5 ± 0.3	2.5 ± 0.3	3.28 ± 0.21	3.2 ± 0.3	0.5 ± 0.3	5.9 ± 0.3	2.01 ± 0.3
Age	$3.2^{+2.1}_{-3.1}$	$1.9^{+1.3}_{-1.8}$	$3.05^{+0.92}_{-0.99}$	5.2 ± 1.9	$11.0^{+2.4}_{-1.6}$	$0.4^{+0.2}_{-0.4}$	$4.2^{+1.8}_{-1.9}$
$\rm Mag_{NUV}$	18.21 ± 0.04	17.63 ± 0.03	17.02 ± 0.03	18.69 ± 0.05	17.03 ± 0.02	17.53 ± 0.02	18.56 ± 0.05
$F_{\rm NUV}$	844^{+45}_{-42}	1306^{+55}_{-52}	3142^{+148}_{-141}	1400^{+95}_{-94}	4147^{+195}_{-190}	7165^{+339}_{-316}	1016^{+76}_{-67}
$\log_{10}(R`_{hk})$	-4.476 ± 0.091	-4.507 ± 0.119	-4.844 ± 0.146	-4.781 ± 0.028	-4.674 ± 0.089	-4.765 ± 0.056	-4.455 ± 0.154
$P_{\rm rot_1}$	$26.37^{+7.17}_{-4.89}$	$17.16^{+3.06}_{-2.62}$	$16.75^{+1.41}_{-4.79}$	$16.62^{+2.1}_{-5.12}$	$85.98^{+132.58}_{-45.19}$	$9.17^{+0.65}_{-2.55}$	$26.73^{+5.34}_{-9.16}$
$P_{\rm rot_2}$	$29.69^{+5.00}_{-5.78}$	$16.20^{+3.06}_{-0.49}$	$19.63^{+3.51}_{-5.39}$	$25.69^{+3.15}_{-8.56}$	$134.42^{+46.32}_{-58.26}$	$13.51^{+5.77}_{-7.40}$	$27.07^{+3.96}_{-6.85}$
$P_{\rm rot_3}$	9.51 ± 2.74	11.65 ± 4.17	25.25 ± 11.28	24.3 ± 5.12	22.8 ± 6.91	24.08 ± 5.85	8.29 ± 3.8
$P_{\rm rot}$	$28.28^{+3.99}_{-3.97}$	$16.93^{+2.02}_{-1.55}$	$17.45^{+2.4}_{-2.85}$	$20.16^{+2.88}_{-4.22}$	$120.1^{+60.46}_{-37.54}$	$10.65^{+3.27}_{-3.01}$	$25.7^{+4.16}_{-4.71}$
M_p	$0.467^{+0.024}_{-0.023}$	$0.564^{+0.026}_{-0.025}$	$0.586^{+0.033}_{-0.032}$	$0.47^{+0.034}_{-0.036}$	$0.487^{+0.052}_{-0.054}$	$0.577^{+0.057}_{-0.056}$	$0.65^{+0.06}_{-0.062}$
R_p	$1.119^{+0.017}_{-0.018}$	$1.232^{+0.014}_{-0.017}$	$1.314^{+0.021}_{-0.025}$	$1.23^{+0.027}_{-0.025}$	$1.177^{+0.028}_{-0.024}$	$1.337^{+0.028}_{-0.033}$	$1.201^{+0.033}_{-0.028}$
$T_{\rm eq}$	1167 ± 96	1217 ± 101	1342^{+111}_{-110}	1350 ± 112	1158 ± 95	1481 ± 123	1230 ± 102
G_p	$9.65^{+0.59}_{-0.56}$	$9.62^{+0.52}_{-0.48}$	$8.8^{+0.59}_{-0.56}$	$8.04^{+0.67}_{-0.71}$	$9.1^{+1.0}_{-1.1}$	$8.36^{+0.92}_{-0.88}$	$11.7^{+1.2}_{-1.3}$
ρ_p	$0.332^{+0.023}_{-0.022}$	$0.301^{+0.019}_{-0.017}$	$0.258^{+0.02}_{-0.019}$	$0.252^{+0.024}_{-0.025}$	$0.299^{+0.037}_{-0.039}$	$0.241^{+0.03}_{-0.028}$	$0.375^{+0.044}_{-0.047}$
I_p	288^{+47}_{-45}	341 ± 68	504^{+96}_{-93}	517^{+127}_{-128}	279 ± 51	748^{+178}_{-174}	356^{+93}_{-87}
$P_{\rm orb}$	3.3610026 $+6.1e{-}7{-}6.3e{-}7$	3.7648337 $\pm1.2e{-}6$	4.465631 $\pm1.3e{-}6$	3.4252567 $\pm1.2e{-}6$	3.7784022 $\pm1.6e{-}6$	3.3726511 $+2.7e{-}6{-}2.9e{-}6$	4.6058827 $\pm1.1e{-}6$
a/R_*	$11.21^{+0.13}_{-0.14}$	11.33 ± 0.14	$10.66^{+0.14}_{-0.15}$	9.13 ± 0.17	$11.2^{+0.17}_{-0.18}$	9.22 ± 0.13	$11.36^{+0.2}_{-0.26}$
t_0	2454596.43260 $+0.000762-0.00075$	2455274.99649 $+0.00100-0.00103$	2455737.93919 $+0.00097-0.00095$	2456258.06272 $+0.00084-0.00088$	2456502.72415 ±0.00102	2457028.58329 $+0.00103-0.00101$	2457031.95666 $+0.00025-0.00026$
b	$0.195^{+0.077}_{-0.114}$	$0.357^{+0.035}_{-0.042}$	$0.235^{+0.067}_{-0.105}$	$0.724^{+0.019}_{-0.02}$	$0.319^{+0.059}_{-0.072}$	$0.619^{+0.027}_{-0.033}$	$0.395^{+0.065}_{-0.055}$
i	$89.0^{+0.59}_{-0.41}$	$88.19^{+0.23}_{-0.2}$	$88.74^{+0.57}_{-0.38}$	85.45 ± 0.2	$88.37^{+0.38}_{-0.33}$	$86.15^{+0.24}_{-0.21}$	$88.01^{+0.3}_{-0.38}$
K	$69.6^{+2.6}_{-2.7}$	$75.3^{+2.5}_{-2.6}$	68.7 ± 3.2	$62.1^{+3.8}_{-3.9}$	$73.1^{+7.6}_{-7.7}$	70.8 ± 6.7	$78.3^{+6.3}_{-6.6}$

Note. The top 15 parameters, delineated by a thicker line, are for the host stars. In order, they are mass [$M_\odot$], radius [$R_\odot$], effective temperature [K], $\log_{10}$ of surface gravity [cgs], density [$\rho_\odot$], $\log_{10}$ of iron to hydrogen abundance relative to the Sun [dex], radial velocity [km s^{-1}], age [Gy], NUV magnitude, NUV flux from the star at the semimajor axis of the planet [Watts m^{-2}], $\log_{10}$ of the calcium H and K indices [dex], rotational period derived from $v \sin I$ ($P_{\rm rot_1}$), photometry ($P_{\rm rot_2}$), R`$_{hk}$ ($P_{\rm rot_3}$), and the adopted rotational period (a weighted mean of the $v \sin I$ and photometry periods, $P_{\rm rot}$) [days]. The following 12 parameters are for the corresponding planet: mass [M_j], radius [R_j], equilibrium temperature [K], surface gravity [m s^{-2}], density [ρ_j], insolation [$I_\oplus$], and orbital period [days], semimajor axes relative to the host stars' radii, reference mid-transit time transit [BJD], impact parameters, orbital inclinations [degrees], and RV semi-amplitude [m s^{-1}], respectively.

used the weighted mean from these two methods as our adopted values, reported in Table 1.

3.1.3. Near-UV Flux

We derived Near-Ultraviolet (NUV) fluxes for each host star using their Galaxy Evolution Explorer (GALEX;

Bianchi & GALEX Team 1999) observations. We obtained GALEX NUV magnitudes from VizieR (II/335) (Bianchi et al. 2017), which can also be accessed via the Mikulski Archive for Space Telescopes (MAST) (STScI 2013). The magnitude was converted to total NUV luminosity using Equation (6) of Schneider & Shkolnik (2018), and Gaia DR3 parallaxes, assuming a central mean wavelength of 2267 Å. We then

converted those magnitudes to flux density as

$$F_{\rm NUV} \left[\frac{\rm erg}{\rm s\,cm^2\,\mathring{A}} \right] = 2.06 * 10^{-16} * 10^{\frac{20.08 - m_{\rm NUV}}{2.5}}, \qquad (2)$$

where $m_{\rm NUV}$ is the observed GALEX AB NUV magnitude. This equation was derived from gsfc.nasa.gov.

3.2. Planetary Parameters

We rederived the parameters of each planet using the SPOC[9] TESS light curves downloaded from MAST 10.17909/fwdt-2x66 and described in Appendix B, and radial velocity observations from CORALIE (Queloz et al. 2000), HARPS (Mayor et al. 2003), and CYCLOPS (Horton et al. 2012). We also used HAT-South (Bakos et al. 2013) data with TESS to fit the transit of HATS-29b because of contamination from a background *RR-Lyrae* star in the TESS data. After removing that contamination (see Appendix C), the TESS and HAT-South transit light curves were modeled using the same procedure as the other six targets. A table summarizing the RV and photometric data is provided in Appendix B.

We jointly fitted the light curves and RVs of each target with Juliet (Espinoza et al. 2019a), initially assuming circular orbits and quadratic limb-darkening coefficients with uniform priors from 0 to 1. All other orbital parameters (P, t_0, a/R^*, Rp/R^*, b, i, K, and ρ_p) were fitted with Gaussian priors set off of the discovery papers' mean and uncertainty values. We then phase-folded the photometric light curves, based on the period of that fit, and removed points that were 3σ deviant from a moving average of 20 points. This resulted in a few percent of data points being removed per sector. The clipped data were then used for the final Juliet joint RV-transit fit.

The equilibrium temperature of each planet, $T_{\rm eq}$, was computed using Equation (1) from Lopez-Morales & Seager (2007) and assuming each planet had the same atmospheric albedo and energy redistribution factors of $A_B = 0.2 \pm 0.1$ and $f = 1/3 \pm 0.1$.[10] To approximate the insolation levels, I_p, reaching each planet, we calculated the bolometric luminosity assuming the stars emit as blackbodies. To compensate for this oversimplification, we increased the obtained uncertainties in each I_p by a factor of three. Because we can also obtain information about stellar densities from the transits, we found the weighted average of the density obtained from the spectral analysis discussed in Section 3.1 and the density obtained from Juliet to produce the values in Table 1. Our updated parameters are on average 2.7 times more precise than previous literature discovery parameters. Figures 2 and 3 show the resulting light-curve and radial velocity fits for each planet.

4. Homogeneous Analysis of Transmission Spectra

Our last step in the process of obtaining parameters as homogeneous as possible for all seven systems was to rederive atmospheric parameters for the three planets in the sample with observed transmission spectra. Those are WASP-6b, observed with VLT/FORS2, HST/STIS G430 and G750, and HST/WFC3 G141 between 0.32 and 1.65 μm (Nikolov et al. 2015;

Carter et al. 2020), WASP-96b observed with VLT/FORS2, Magellan/IMACS, and HST/WFC3 G102 and G141 between 0.4 and 1.64 μm (Nikolov et al. 2018; Yip et al. 2021; McGruder et al. 2022; Nikolov et al. 2022), and WASP-110b observed with VLT/FORS2 between 0.4 and 0.83 μm (Nikolov et al. 2021).

A retrieval analysis of the WASP-96b data was recently done by McGruder et al. (2022), using Platon (Zhang et al. 2019) and Exoretrievals (Espinoza et al. 2019b). For consistency, we did a similar analysis for the transmission spectra of WASP-6b and WASP-110b. That is, with Exoretrievals we tested models including water, potassium, sodium, stellar activity, or scattering features and the different combinations of each. With Platon, we tested models with scatters or stellar activity, where Platon assumes equilibrium chemistry and fits for the C/O ratio and planetary metallicity to extrapolate the abundances of atomic/molecular species. The ln Z Bayesian evidences were used to favor one model over another. We considered a difference in ln Z greater than 2.5 between two models to be moderately significant, and greater than 5 to strongly support the model with higher lnZ (Trotta 2008; Benneke & Seager 2013). Additionally, we used Table 2 and Equation (2) from Rackham et al. (2019), to limit the contribution of stellar activity to inhomogeneity covering fractions of $4.1\% \pm 4.1\%$ when both spots and faculae are present.

The priors of each retrieval for both WASP-6b and WASP-110b and the Bayesian evidences relative to a flat (for Exoretrievals) or clear (for Platon) spectrum are shown in Appendix D. The highest-evidence models for both targets with both retrievals were ones that included activity, which is consistent with what was found in previous analyses (Nikolov et al. 2015; Carter et al. 2020; Nikolov et al. 2021). Exoretrievals also found significant evidence for water and a sodium feature in the WASP-6b spectrum, which was not found for WASP-110b. The features found in the WASP-6 data are muted, indicative of high-altitude aerosols. Activity could not explain the muted features; in fact, with the unocculted cooler spots that the retrievals find, the sodium signal would be enhanced. This can be seen in Figure 9 of Carter et al. (2020). Furthermore, the cloud deck pressures of ~0.1 bars suggest WASP-6b has substantially more aerosols than WASP-96b, where its models favor a cloud deck pressure of ~20 bars. WASP-110b's spectrum is more extreme than WASP-6b's, where all atomic features are missing and a cloud deck pressure of ~0.03 mbars is suggested—although it is not well-constrained, due to the lack of features.

5. Search for Trends

Using the new set of homogeneously derived parameters described in Sections 3 and 4, we searched for correlations between system parameters and what we define as *aerosol levels* in the transmission spectrum of the planets.

We quantify *aerosol levels* using as proxy the amplitude of the Na I doublet at 5892.9 $\mathring{A}$ in the transmission spectra of WASP-6b, WASP-96b, and WASP-110b. This was calculated as the sum of transit bins within a narrow range centered on the Na I doublet (5862.9–5892.9 $\mathring{A}$) minus the sum of bins blueward and redward of this region, while also being outside of the wings of the sodium feature. For WASP-96b, these ranges were 4880 to 5380 $\mathring{A}$ and 6200–6700 $\mathring{A}$, but they were

---

[9] Science Processing Operations Center (Jenkins et al. 2016).

[10] A_B is based on geometric albedos measured for other hot Jupiters (e.g., Mallonn et al. 2019; Adams et al. 2022; Blažek et al. 2022), and f is based on the expectation that gas giants with lower incident flux tend to have more efficient heat redistribution (Perez-Becker & Showman 2013; Komacek & Showman 2016; Komacek et al. 2017).
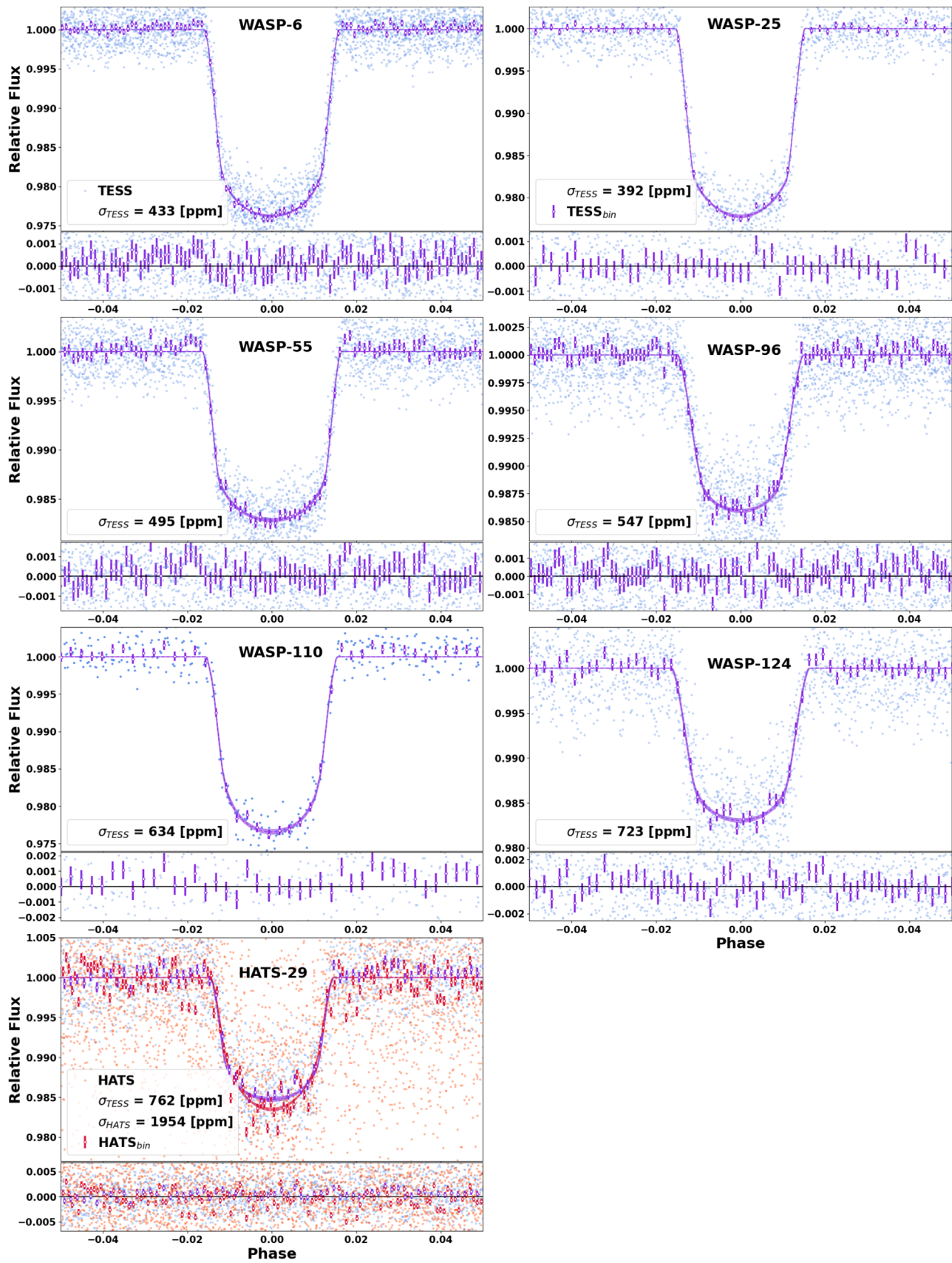
Figure 2. The phase-folded transit data for each of the similar seven systems and their `Juliet` best-fit transit models (dotted lines). 1σ uncertainties of the fits are shaded in the same color as the transit models. The plotted "bin" data have 30-point binning, aside for WASP-110, which has eight-point binning.
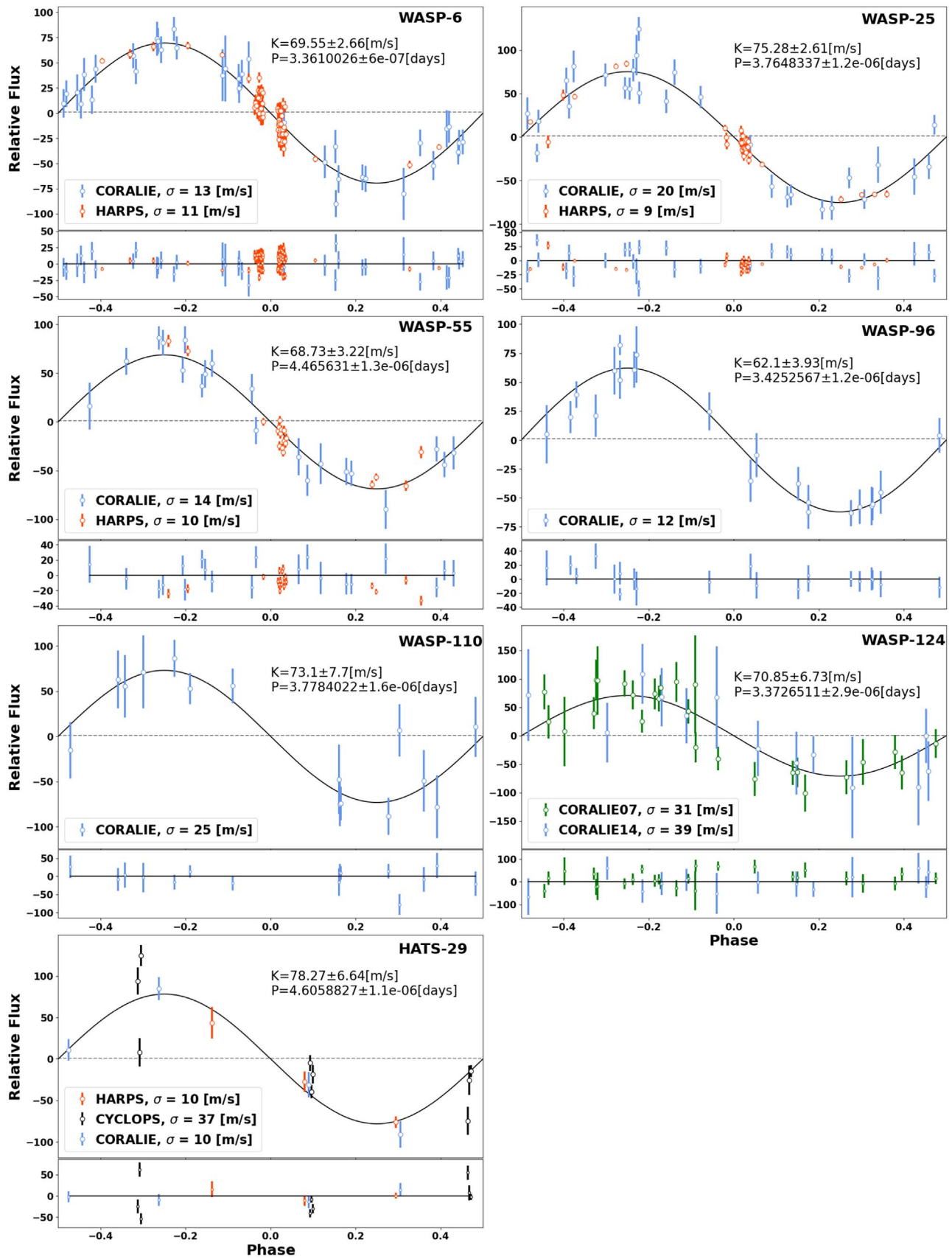
Figure 3. The phase-folded RV data of each of the similar seven systems and their `Juliet` best-fit RV models (solid black lines). The HARPS RV measurements that were during transit were omitted. For WASP-124b, "CORALIE07" and "CORALIE14" represent observations taken before/after the CORALIE upgrade (see Maxted et al. 2016).
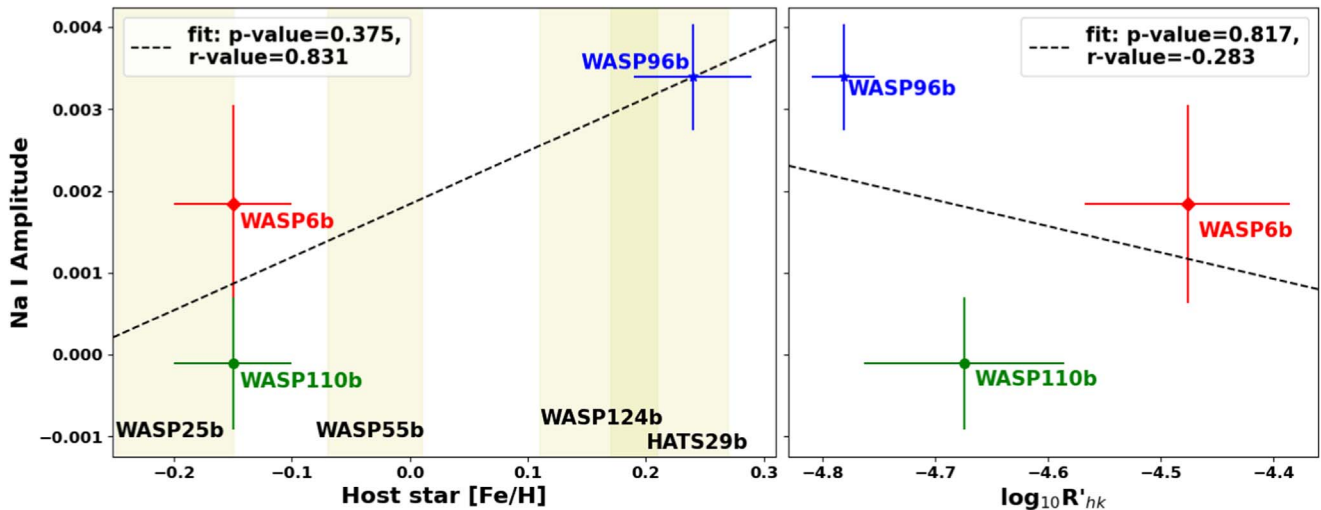
Figure 4. Left: Sodium amplitude vs. host star metallicity from the observed WASP-6b (red diamond), WASP-96b (blue star), and WASP-110b (green circle) transmission spectra. The best-fit linear regression (black dashes) has a Pearson's correlation coefficient, *r-value*, of 0.831. The metallicity ranges WASP-25b, WASP-55b, WASP-124b, and HATS-29b cover are plotted as yellow shaded regions. Right: Same as left, but with Na amplitude vs. $\log_{10}(R'_{HK})$. Here, the r-value to the best-fit linear regression does not support a correlation of the Na amplitude to $\log_{10}(R'_{HK})$.

Table 2
Summary of the Photometric and RV Data

Star	Transit data		ASAS-SN			RV data		
	Sectors	Transits	Filter	Date range	Obs.	Spectrograph	Obs.	Source
WASP-6	2, 29	13	V	2013-11-25 to 2018-11-26	883	CORALIE	35	Gillon et al. (2009)
			g	2017-09-16 to 2022-04-18	2073	HARPS	55	Trifonov et al. (2020)
WASP-25	10	6	V	2012-01-24 to 2018-08-20	820	CORALIE	28	Brown et al. (2012)
			g	2017-12-21 to 2022-04-18	2401	HARPS	31	Trifonov et al. (2020)
WASP-55	10, 37	8	V	2012-02-17 to 2018-08-19	961	CORALIE	20	Hellier et al. (2012)
			g	2017-12-16 to 2022-04-19	2156	HARPS	19	Trifonov et al. (2020)
WASP-96	2, 29	13	V	2014-04-30 to 2018-09-24	921	CORALIE	21	Hellier et al. (2014)[a]
			g	2017-09-05 to 2022-02-10	2592			
WASP-110	27	6	V	2014-04-29 to 2018-09-24	916	CORALIE	15	Anderson et al. (2014)[a]
			g	2017-09-05 to 2022-04-18	2286			
WASP-124	1	8	V	2014-04-30 to 2018-09-19	1577	CORALIE	39	Maxted et al. (2016)[a]
			g	2017-09-07 to 2022-04-18	4217			
HATS-29	13	6	V	2014-05-17 to 2018-09-24	989	HARPS	3	Espinoza et al. (2016)
(*HAT-South*			g	2017-10-03 to 2022-04-18	2165	CYCLOPS	9	Espinoza et al. (2016)
data:)	⋯	23				CORALIE	4	Espinoza et al. (2016)

Notes. The HAT-South photometric data for HATS-29 (first columns, last row) were acquired from Bakos et al. (2013). Trifonov et al. (2020) reanalyzed archival HARPS data using SERVAL (Zechmeister et al. 2018). The number of observations is denoted "Obs." and consists of the unbinned/unclipped observations for the ASAS-SN data.
[a] Data obtained through DACE.

5340–5820 Å and 5960–6440 Å for WASP-6b and WASP-110b, which did not have notable absorption wings.

The result of our search for correlations between aerosol levels and system parameters is summarized in Figure 4. We find a significant correlation between the amplitude of the Na I feature in the transmission spectrum of the planet and the overall [Fe/H] of the host star. The linear fit to this trend has a Pearson correlation coefficient of $r = 0.83$, corresponding to a 99% confidence of a found correlation. To examine if there could be a correlation with stellar activity, we used $\log_{10}(R'_{HK})$ (see Section 3.1.1). The best linear fit to $\log_{10}(R'_{HK})$ and the

Na I signal has $r = -0.28$, corresponding to about 24% confidence that there is such a correlation. Therefore, we find no correlation with $\log_{10}(R'_{HK})$. However, the chromospheric activity measured from $\log_{10}(R'_{HK})$ is not a direct measurement of total high-energy flux (e.g., see Zhang et al. 2020; Johnstone et al. 2021), where total high-energy emission is likely the more important parameter affecting aerosol formation rates (Moses et al. 2011, 2013; Fleury et al. 2019). Thus, we need more direct measurements of the host stars' high-energy levels (e.g., HST/UVIS or XMM-Newton observations) to confidently rule out such a correlation.

6. Summary and Conclusions

We have identified seven systems that have very similar characteristics to one another, the "*Similar Seven*," where the host star metallicity is the only stark difference between the parameters measured for these systems. Three of the planets in this sample already have transmission spectra observed, and though they have similar parameters, their transmission spectra have widely varying amounts of high-altitude aerosols obscuring features. To thoroughly search for correlations between the observed spectra aerosol levels and system parameters, we homogenously reanalyze HARPS and FEROS stellar spectra, as well as HARPS, CORALIE, and CYCLOPS RV data with TESS and HAT-South transit data to refine the stellar and transit parameters. We found that host star metallicity seems to correlate with the observed aerosol levels, with a 99% confidence that a linear correlation exists, implying that planets around higher-metallicity stars would have lower high-altitude aerosol levels. If this holds, it could be explained by the requirement of viable *seed* particles needing to be lofted to high enough altitudes for cloud forming gases to condense on (e.g., Helling 2008, and references therein). The higher metallicity might cause the formed *seed* particles to be more dense and subsequently differentiate lower in the atmosphere. However, given that the potential trend was found with only the three observed transmission spectra, the correlation is tentative, pending further observations of the other sample planets.

We also use $\log_{10}(R'_{HK})$ as a proxy to explore if high-energy irradiation could be correlated to the differences in the transmission spectra, given that there are no direct measurements of the stars' high-energy emissions. We found no clear signs of a correlation with this parameter. However, correlation to the host star's high-energy levels may still be present and require more direct measurements, i.e., with XMM-Newton and/or HST/UVIS.

Regardless of whether metallicity or high-energy irradiation is found to be a contributing factor to high-altitude aerosols in these system, the *similar seven* planets are ideal targets for understanding the unique physical and chemical processes undergoing in these class of planets: this is because, due to the similarity of most parameters, they act as a controlled sample. This approach of specifically selecting very similar targets should be a common practice in exoplanet atmosphere studies, and has the potential to isolate key physical or chemical phenomena.

Appendix A
Stellar Rotation Axis Distribution

For WASP-6, there are two measurements of the rotation axis alignment, λ, i.e., the angle between the planet's orbital axis and the rotation axis of the star: $\lambda = 11^{+14°}_{-18}$, obtained using the Rossiter–McLaughlin effect (Gillon et al. 2009) and $\lambda = 7°.2 \pm 3°.7$ (which we adopt), obtained using occulted star spots (Tregloan-Reed et al. 2015). For WASP-25, Brown et al. (2012) measured a λ of $14°.6 \pm 6°.7$ via Rossiter–McLaughlin. The other five stars in our sample do not have direct λ measurements, so instead we calculated their most likely λ values using the distribution of λ values measured for G-type stars, i.e., with $T_{eff} \in [5300, 6300]$ K, as shown in Figure 5. Seventy-five percent of the λ values are less that $\pm 20°$, suggesting that the bulk of exoplanet systems with G-type host stars are aligned. This is in agreement with the findings of Triaud (2018) (see their Figure 6). Based on the distribution of values in Figure 5, we adopt a $\lambda = 0° \pm 30°$ for the remaning five systems in our sample. The estimated rotation periods for all our targets, computed using Equation (1), are listed in Table 1.
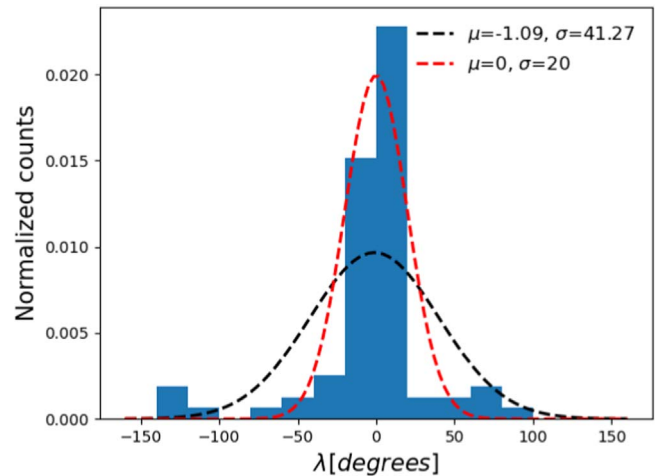

Figure 5. The distribution of observed λ values of 80 exoplanet systems with the host star between 5300 and 6300 K, obtained through `TEPCat`.[11] Here, $\lambda = 0°$ means the axes are fully aligned. The bulk of the λ values are smaller than $\pm 20°$, suggesting alignment of the orbital and spin axes. Two Gaussians are overplotted: one with the wide distribution ($\sigma = 41.3$, black) and one with a narrow distribution ($\sigma = 20$, red). We adopt a mean distribution of $\lambda = 0° \pm 30°$.

Appendix B
Stellar Rotation Periods from TESS and ASAS-SN Light Curves

We downloaded the TESS SPOC[12] light curves for each target from MAST 10.17909/fwdt-2x66. The TESS sectors and observed number of transits for each target are summarized in Table 2. We also downloaded ASAS-SN (Shappee et al. 2014; Kochanek et al. 2017) time series observations for each target in *V*- and *g*-bands, which are treated as separate photometric monitoring campaigns. The number of ASAS-SN observations per photometric band, for each target are also summarized in Table 2.

We used the time series observations above to estimate the rotation period of each star following a method of analysis similar to the one described in McGruder et al. (2020). For the TESS data, we masked all the in-transit points using the known ephemerides of each planet, to search for photometric modulations of the stars themselves. Before searching for photometric modulations, we binned the data for each target in 3.33 hr bins (16.66 hr bins for WASP-110). Given that the expected rotation periods for all the stars are longer than 10 days, those binning levels should not affect results. For the ASAS-SN data, we sigma-clipped observations that deviated by more than 3σ from the overall mean of each light curve, obtained the weighted average of all observations for a given night (typically three observations per night), and removed observations with uncertainties three times larger than the mean uncertainty.

To search for the $P_{\rm rot}$ of each star, we jointly modeled all the photometric data sets for each target using `Juliet`'s (Espinoza et al. 2019a) Gaussian processes (GP) semi-periodic

kernel, setting the GP characteristic timescale and period as common terms between all data sets. The other parameters (jitter term, GP amplitude, and GP constant scale term) were specific to the individual data sets. Also, when data from more than one TESS sector were available, we combined them and modeled them together. We modeled activity as a semi-periodic GP instead of using periodograms because it has been found that peaks inconsistent with the rotational period of stars can appear in the latter (Haywood et al. 2014; Nava et al. 2020). We assume the main driving factor for the GP period is stellar inhomogeneities coming in and out of view as the star rotates, and therefore we call this the rotation period, $P_{\rm rot}$. The priors for $P_{\rm rot}$ were set using the $v \sin I$ of each star from Section 3.1. For all the targets but WASP-124 and HATS-29, we used normal priors with mean and standard deviations near the values derived from $v \sin I$. For WASP-124, we used a normal prior truncated at 5 days to prevent sampling of unrealistically low periods driven by the TESS data. For HATS-29, we used a uniform distribution between 17 and 33 days for the same reason.

The advantage of the TESS data is the continuous monitoring with high photometric precision. However, given that it only monitors a sector for about 24 days, the long baseline of the ASAS-SN data complements TESS well. This emphasizes the advantage of a joint fit with all photometric data, but we also run the TESS and ASAS-SN data separately (with the same priors) to outline the contribution from each monitoring source. Table 3 shows the period, amplitude, and median absolute deviations (MAD) of both photometric monitoring sources.

Finally, to ensure that the found rotation periods were not driven by the sampling of the data, we tested their window

Table 3
Summary of TESS and ASAS-SN Photometric Monitoring `Juliet` Fits

Star	TESS			ASAS-SN				Joint	
	MAD (ppm)	Period (days)	Amplitude (ppm)	MAD_g (ppm)	MAD_v (ppm)	Period (days)	Amplitude (ppm)	Period (days)	Amplitude (ppm)
WASP-6	348.5	$28.93^{+6.63}_{-6.9}$	0.23	2407.3	2266.2	$28.37^{+5.58}_{-7.19}$	1383.1	$29.69^{+5.00}_{-5.78}$	57.3
WASP-25	376.8	$18.11^{+2.82}_{-2.99}$	187.9	1847.6	1459.3	$16.11^{+1.73}_{-0.63}$	947.2	$16.20^{+3.06}_{-0.49}$	199.5
WASP-55	241.2	$19.46^{+3.77}_{-3.87}$	132.4	1516.3	2494.4	$15.54^{+6.36}_{-3.21}$	1181.2	$19.63^{+3.51}_{-5.39}$	49.1
WASP-96	230.0	$19.85^{+5.05}_{-5.84}$	58.7	1955.89	1761.3	$15.38^{+10.78}_{-2.78}$	703.8	$25.69^{+3.15}_{-8.56}$	98.1
WASP-110	330.6	$112.2^{+52.4}_{-47.6}$	48.0	2063.9	2220.8	$132.9^{+43.6}_{-71.1}$	488.1	$134.42^{+46.32}_{-58.26}$	58.8
WASP-124	447.3	$12.04^{+4.84}_{-6.0}$	256.4	1427.5	1441.3	$10.98^{+4.44}_{-3.21}$	714.6	$13.51^{+5.77}_{-7.40}$	340.1
HATS-29	737.5	$26.06^{+4.79}_{-5.78}$	78.3	1775.7	2340.9	$20.78^{+9.063}_{-0.585}$	1654.5	$27.07^{+3.96}_{-6.85}$	90.1

Note. The MAD is for the binned data. The amplitdues are obtained by using `scipy.optimize.minimize` (Virtanen et al. 2020) to fit a sine curve to the data phase-folded on the `Juliet` best-fit period. The subscripts *g* and *v* on the ASAS-SN MAD correspond to the *g*- and *V*-band filters.

functions, where we used all time stamps of monitoring data but set the flux and uncertainties to 0. Doing this suggested no periodic signal due to the observing cadence. The P_{rot} values for each system are listed in Table 1.

Appendix C
HATS-29 TESS Light-curve Decontamination

Because of the low image resolution of TESS, the light curve of HATS-29 is contaminated by a background *RR-Lyrae* star (see top panel of Figure 6). We isolated the RR-Lyrae signal by first excluding the in-transit data (using transit parameters from Espinoza et al. 2016), then applying a Lomb–Scargle periodigram (Lomb 1976; Scargle 1982) analysis to this out-of-transit data to find a period of 0.631 days. Next, we phase-folded the data to the 0.631 d period, binned the data by 100 points, and finally smoothed the binned data with `scipy.signal.savgol_filter` (Virtanen et al. 2020)[13] using a window set to 51 and an order of 10. Our phase-folded data and corresponding RR-Lyrae model can be seen in the second panel of Figure 6. We then subtracted (in magnitude space) the
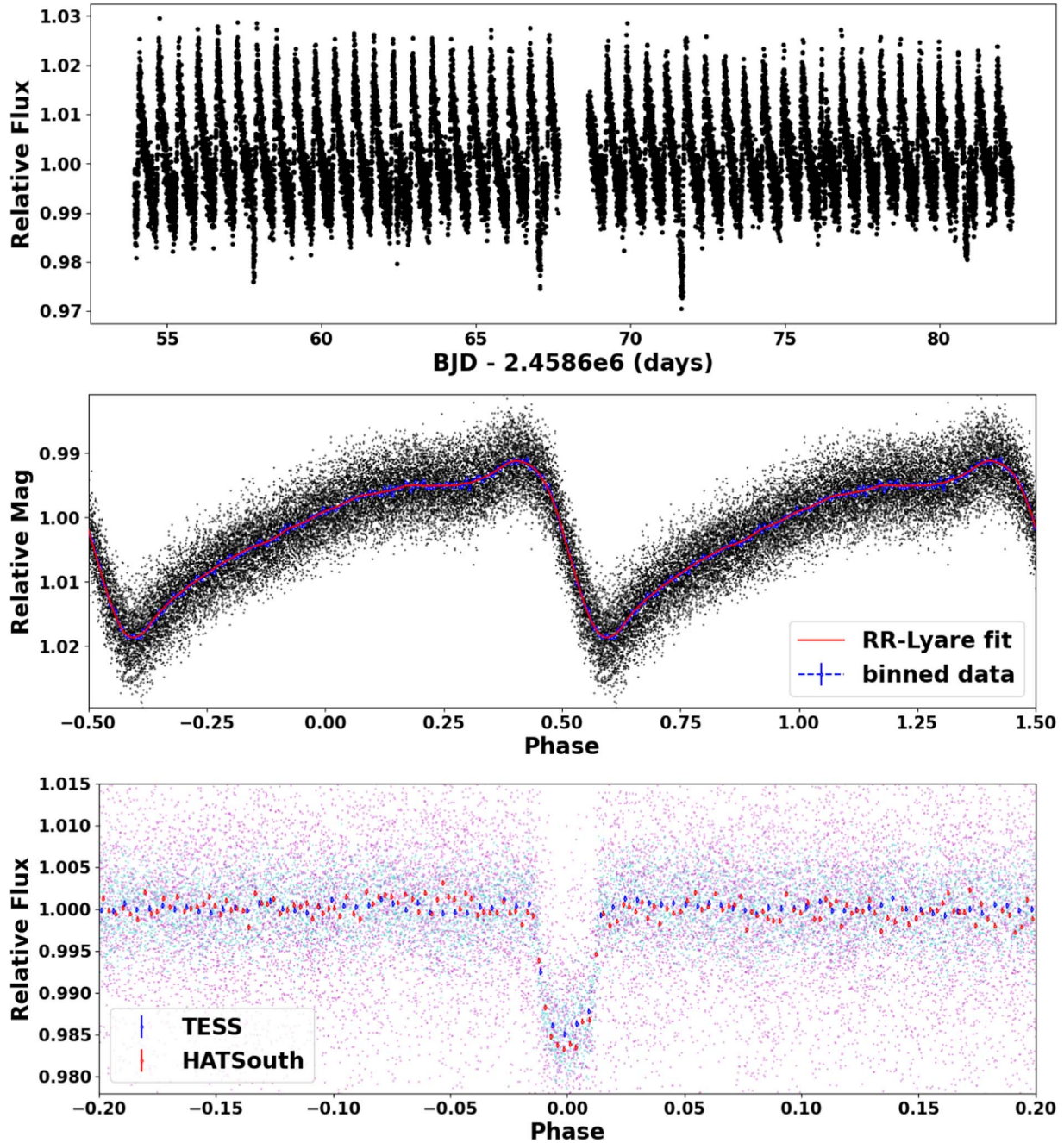

Figure 6. Top: The TESS SPOC of TIC 201604954, extracted from MAST 10.17909/fwdt-2x66, which was observed in sector 13. From visual inspection, one can see that the RR-Lyrae oscillations dominate, with 43 complete oscillations observed. Middle: The same data after removing the HATS-29b transits and phase-folding on a period of 0.631343 days, which corresponds to the background RR-Lyrae's period. Here, black represents all phase-folded observations, blue represents the data binned by 100, and red represents the `savitzky_golay` smoothed fit. Bottom: The TESS data after modeling out the RR-Lyrae features, doing the same sigma clipping done for every other target (see Section 3.2). Here, cyan is used to show the unbinned data, and blue shows the same data binned by 100. Overplotted are the HAT-South data, where magenta and red are used to indicate the unbinned and binned data, respectively. For both light curves we used a P and t_0 of 4.60588 and 2457031.957, respectively.

best RR-Lyrae light-curve model from the TESS data, and reduced the corrected TESS data with the same procedures of the other TESS observations (see Appendix B).

HAT-South (Bakos et al. 2013) has public light curves for HATS-29, which we downloaded from the survey's website,[14] and is not contaminated by the background star. We compared the best-fit `Juliet` transit with TESS against a fit with the HAT-South data. Upon confirming that the transit parameters —aside from transit depth, which one would expect to differ due to the different photometric bands—were consistent with

each other, we ran a joint `Juliet` fit with all the transit and RV data to obtain our final planetary parameters of this system. See the bottom panel of Figure 6 for an overlay of the TESS and HAT-South data.

Appendix D
Atmospheric Retrieval Results

Table 4 has the priors used for each model and the $\Delta \ln Z$ of each retrieval run are in Table 5.

Table 4
The Priors for `Exoretrievals` and `PLATON`

	Exoretrievals			PLATON	
Parameter	Function	Bounds	Parameter	Function	Bounds
reference pressure (P_0, bars)	log-uniform	−8 to 3	reference pressure (P_{clouds}, Pa)	log-uniform	−3.99 to 7.99
planetary atmospheric temperature (T_p)	uniform	600–1800 K	planetary atmospheric temperature (T_{p})	uniform	600–1800 K
stellar temperature (T_{occ})	uniform	T_{eff}–240 to T_{eff}+240 K	stellar temperature (T_{star})	Gaussian	$\mu = T_{\mathrm{eff}}$, $\sigma = 150$ K
stellar heterogeneities temperature (T_{het})	uniform	T_{eff}–3000 to T_{eff}+3000 K	stellar heterogeneities temperature (T_{spot})	uniform	T_{eff}–3000 to T_{eff}+3000 K
heterogeneity covering fraction (f_{het})	Gaussian	$\mu = 0.041$, $\sigma = 0.041$	heterogeneity covering fraction (f_{spot})	Gaussian	$\mu = 0.041$, $\sigma = 0.041$
haze amplitude (a)	log-uniform	−30 to 30	scattering factor	log-uniform	−10 to 10
haze power law (γ)	uniform	−14 to 4	scattering slope (α)	uniform	−4 to 14
log cloud absorbing cross-section (σ_{cloud})	uniform	−80 to 80	metallicity ($Z/Z_{\odot}$)	log-uniform	−1 to 3
trace molecules' mixing ratios	log-uniform	−30 to 0	C/O	uniform	0.05 to 2
reference radius factor (f)	uniform	0.8 to 1.2	1 bar, reference radius (R_0)	uniform	R_p−.2R_p to R_p+.2R_p

Note. These priors were set to allow for a wide parameter space to be surveyed, but contained within physical regimes. Not all parameters were included in each model fit (see Table 5). We used 5000 live points for all runs. For further description of the parameters of `Exoretrievals`, please refer to Appendix D of Espinoza et al. (2019b). T_{eff} is the effective temperature of the host star, which is 5438 and 5392 K for WASP-6 and WASP-110, respectively. γ is the exponent of the scattering slope power law, where −4 is a Rayleigh scattering slope. α is the wavelength dependence of scattering, with 4 being Rayleigh. f is a factor multiplied by the inputted planetary radius to produce the reference radius, i.e., $R_0 = fR_p$, where R_p is the radius of the planet, corresponding to $1.119R_j$ and $1.177R_j$ for WASP-6b and WASP-110b, respectively.

Table 5
Δln Z for `Exoretrievals` (left) and `PLATON` (right) Retrievals

	Exoretrievals						PLATON	
Model:	flat	H_2O	Na	K	$H_2O + Na$	$H_2O + K + Na$	Model:	
WASP-6b:								
clear	0.0	1.47	3.79	70.32	70.26	71.7	clear	0.0
scatterers	⋯	69.96	70.14	69.95	69.15	69.9	scattering	10.09
activity	84.21	93.85	88.03	90.53	96.07	97.44	activity	13.49
Both	⋯	81.1	82.35	81.59	81.49	81.97	Both	12.91
WASP-110b:								
clear	0.0	0.15	−1.0	−0.97	−0.14	−0.57	clear	0.0
haze+clouds	⋯	−3.21	−3.09	−3.12	−3.46	−3.6	scattering	2.93
activity	4.35	2.69	2.33	2.39	2.2	1.73	activity	4.08
Both	⋯	−0.08	−0.15	−0.32	−0.43	−1.0	Both	4.15

Note. The Δln Z values are relative to a clear (and flat for `Exoretrievals`'s case) spectrum with the WASP-6b (top) spectrum that included the VLT/FORS2, HST/STIS, and HST/WFC3 data, and the WASP-110b (bottom) spectrum consisting of the VLT/FORS2 data. For WASP-6b, the retrievals with water and sodium were heavily supported by `Exoretrievals`, where including potassium did not make a significant difference in Δln Z. The `PLATON` models that included scattering and activity were supported equally as well as the models with just activity. For WASP-110b, the models with activity were supported, with `Exoretrievals` finding no significant contribution from atomic/molecular species.

ORCID iDs

Chima D. McGruder ● https://orcid.org/0000-0002-6167-3159
Mercedes López-Morales ● https://orcid.org/0000-0003-3204-8183
Rafael Brahm ● https://orcid.org/0000-0002-9158-7315
Andrés Jordán ● https://orcid.org/0000-0002-5389-3944

References

Adams, D. J., Kataria, T., Batalha, N. E., Gao, P., & Knutson, H. A. 2022, ApJ, 926, 157
Ahrer, E., Wheatley, P. J., Kirk, J., et al. 2022, MNRAS, 510, 4857
Alam, M. K., López-Morales, M., MacDonald, R. J., et al. 2021, ApJL, 906, L10
Alam, M. K., López-Morales, M., Nikolov, N., et al. 2020, AJ, 160, 51
Ambikasaran, S., Foreman-Mackey, D., Greengard, L., Hogg, D. W., & O'Neil, M. 2015, ITPAM, 38, 252
Anderson, D. R., Brown, D. J. A., Collier Cameron, A., et al. 2014, arXiv:1410.3449
Astropy Collaboration, Robitaille, T. P., Tollerud, E. J., et al. 2013, A&A, 558, A33
Bakos, G. Á., Csubry, Z., Penev, K., et al. 2013, PASP, 125, 154
Benneke, B., & Seager, S. 2013, ApJ, 778, 153
Bianchi, L. & GALEX Team 1999, MmSAI, 70, 365
Bianchi, L., Shiao, B., & Thilker, D. 2017, yCat, II/335
Blanco-Cuaresma, S. 2019, MNRAS, 486, 2075
Blanco-Cuaresma, S., Soubiran, C., Heiter, U., & Jofre, P. 2014, A&A, 569, A111
Blažek, M., Kabáth, P., Piette, A. A. A., et al. 2022, MNRAS, 513, 3444
Brahm, R., Espinoza, N., Jordan, A., et al. 2019, AJ, 158, 45
Brahm, R., Jordán, A., & Espinoza, N. 2017a, PASP, 129, 034002
Brahm, R., Jordán, A., Hartman, J., & Bakos, G. 2017b, MNRAS, 467, 971
Brahm, R., Nielsen, L. D., Wittenmyer, R. A., et al. 2020, AJ, 160, 235
Bressan, A., Marigo, P., Girardi, L., et al. 2012, MNRAS, 427, 127
Brown, D. J. A., Cameron, A. C., Anderson, D. R., et al. 2012, MNRAS, 423, 1503
Buchner, J., Georgakakis, A., Nandra, K., et al. 2014, A&A, 564, A125
Carter, A. L., Nikolov, N., Sing, D. K., et al. 2020, MNRAS, 494, 5449
Dymont, A. H., Yu, X., Ohno, K., et al. 2022, ApJ, 937, 90
Enoch, B., Cameron, A. C., Anderson, D. R., et al. 2011, MNRAS, 410, 1631
Espinoza, N., Bayliss, D., Hartman, J. D., et al. 2016, AJ, 152, 108
Espinoza, N., Kossakowski, D., & Brahm, R. 2019a, MNRAS, 490, 2262
Espinoza, N., Rackham, B. V., Jordán, A., et al. 2019, MNRAS, 482, 2065
Feroz, F., Hobson, M. P., & Bridges, M. 2009, MNRAS, 398, 1601
Fleury, B., Gudipati, M. S., Henderson, B. L., & Swain, M. 2019, ApJ, 871, 158
Foreman-Mackey, D. 2016, JOSS, 1, 24
Foreman-Mackey, D., Hogg, D. W., Lang, D., & Goodman, J. 2013, PASP, 125, 306
Fu, G., Deming, D., Knutson, H., et al. 2017, ApJL, 847, L22
Gaia Collaboration, Brown, A. G. A., Vallenari, A., et al. 2018, A&A, 616, A1
Gao, P., Wakeford, H. R., Moran, S. E., & Parmentier, V. 2021, JGRE, 126, e06655
Gillon, M., Anderson, D. R., Triaud, A. H. M. J., et al. 2009, A&A, 501, 785
Harris, C. R., Millman, K. J., van der Walt, S. J., et al. 2020, Natur, 585, 357
Haywood, R. D., Collier Cameron, A., Queloz, D., et al. 2014, MNRAS, 443, 2517
Hellier, C., Anderson, D. R., Cameron, A. C., et al. 2014, MNRAS, 440, 1982
Hellier, C., Anderson, D. R., Collier Cameron, A., et al. 2012, MNRAS, 426, 739
Helling, C. 2008, in ASP Conference Ser. 398, Extreme Solar Systems, ed. D. Fischer et al. (San Francisco, CA: ASP), 443
Helling, C. 2019, AREPS, 47, 583
Heng, K. 2016, ApJL, 826, L16
Horton, A., Tinney, C. G., Case, S., et al. 2012, Proc. SPIE, 8446, 84463A
Hunter, J. D. 2007, CSE, 9, 90
Jenkins, J. M., Twicken, J. D., McCauliff, S., et al. 2016, Proc. SPIE, 9913, 99133E
Johnstone, C. P., Bartel, M., & Gudel, M. 2021, A&A, 649, A96
JWST Transiting Exoplanet Community ERS team, Ahrer, E. M., Alderson, L., et al. 2022, Natur, https://www.nature.com/articles/s41586-022-05269-w#citeas
Kirk, J., Lopez-Morales, M., Wheatley, P. J., et al. 2019, AJ, 158, 144
Kochanek, C. S., Shappee, B. J., Stanek, K. Z., et al. 2017, PASP, 129, 104502
Komacek, T. D., & Showman, A. P. 2016, ApJ, 821, 16
Komacek, T. D., Showman, A. P., & Tan, X. 2017, ApJ, 835, 198
Kreidberg, L. 2015, PASP, 127, 1161
Lomb, N. R. 1976, Ap&SS, 39, 447
Lopez-Morales, M., & Seager, S. 2007, ApJL, 667, L191
Lovis, C., Dumusque, X., Santos, N. C., et al. 2011, arXiv:1107.5325
Mallonn, M., Kohler, J., Alexoudi, X., et al. 2019, A&A, 624, A62
Marley, M. S., Ackerman, A. S., Cuzzi, J. N., & Kitzmann, D. 2013, in Comparative Climatology of Terrestrial Planets, ed. S. J. Mackwell et al. (Tucson: Univ. Arizona Press), 367
Maxted, P. F. L., Anderson, D. R., Collier Cameron, A., et al. 2016, A&A, 591, A55
Mayor, M., Pepe, F., Queloz, D., et al. 2003, Msngr, 114, 20
McGruder, C. D., López-Morales, M., Espinoza, N., et al. 2020, AJ, 160, 230
McGruder, C. D., López-Morales, M., Kirk, J., et al. 2022, AJ, 164, 134

---

[11] https://www.astro.keele.ac.uk/jkt/tepcat/obliquity.html
[12] Science Processing Operations Center (Jenkins et al. 2016).
[13] We used an older version, "`savitzky_golay`", which is the same algorithm before it was included in scipy.
[14] hatsouth.org

Mordasini, C., Klahr, H., Alibert, Y., Benz, W., & Dittkrist, K.-M. 2010, arXiv:1012.5281

Moses, J. I., Madhusudhan, N., Visscher, C., & Freedman, R. S. 2013, ApJ, 763, 25

Moses, J. I., Visscher, C., Fortney, J. J., et al. 2011, ApJ, 737, 15

NASA Exoplanet Science Institute 2019, Transmission Spectroscopy Table, Last Accessed: 2022-05-29, IPAC, doi:10.26133/NEA10

NASA Exoplanet Science Institute 2021, Planetary Systems Composite Parameters Table, NExScI-Caltech/IPAC, Version: 2021-11-17, doi:10.26133/NEA13

Nava, C., López-Morales, M., Haywood, R. D., & Giles, H. A. C. 2020, AJ, 159, 23

Nikolov, N., Maciejewski, G., Constantinou, S., et al. 2021, AJ, 162, 88

Nikolov, N., Sing, D. K., Burrows, A. S., et al. 2015, MNRAS, 447, 463

Nikolov, N., Sing, D. K., Fortney, J. J., et al. 2018, Natur, 557, 526

Nikolov, N. K., Sing, D. K., Spake, J. J., et al. 2022, MNRAS, 515, 3037

Noyes, R. W., Hartmann, L. W., Baliunas, S. L., Duncan, D. K., & Vaughan, A. H. 1984, ApJ, 279, 763

Perez-Becker, D., & Showman, A. P. 2013, AGUFM, 2013, A23B

Queloz, D., Mayor, M., Weber, L., et al. 2000, A&A, 354, 99

Rackham, B. V., Apai, D., & Giampapa, M. S. 2019, AJ, 157, 96

Ricker, G. R., Winn, J. N., Vanderspek, R., et al. 2014, Proc. SPIE, 9143, 914320

Scargle, J. D. 1982, ApJ, 263, 835

Schneider, A. C., & Shkolnik, E. L. 2018, AJ, 155, 122

Shappee, B. J., Prieto, J. L., Grupe, D., et al. 2014, ApJ, 788, 48

Sing, D. K., Fortney, J. J., Nikolov, N., et al. 2016, Natur, 529, 59

Speagle, J. S. 2020, MNRAS, 493, 3132

Stahl, O., Kaufer, A., & Tubbesing, S. 1999, in ASP Conf. 188, Optical and Infrared Spectroscopy of Circumstellar Matter, ed. B. Guenther, B. Stecklum, & S. Klose (San Francisco, CA: ASP), 331

Stevenson, K. B. 2016, ApJL, 817, L16

STScI 2013, GALEX/MCAT, STScI/MAST, doi:10.17909/T9H59D

Suárez Mascareño, A., Rebolo, R., & González Hernández, J. I. 2016, A&A, 595, A12

Tregloan-Reed, J., Southworth, J., Burgdorf, M., et al. 2015, MNRAS, 450, 1760

Triaud, A. H. M. J. 2018, in Handbook of Exoplanets, ed. H. J. Deeg & J. A. Belmonte (Cham: Springer), 2

Trifonov, T., Tal-Or, L., Zechmeister, M., et al. 2020, A&A, 636, A74

Trotta, R. 2008, ConPh, 49, 71

Tsiaras, A., Waldmann, I. P., Zingales, T., et al. 2018, AJ, 155, 156

Virtanen, P., Gommers, R., Oliphant, T. E., et al. 2020, NatMe, 17, 261

Wakeford, H. R., Wilson, T. J., Stevenson, K. B., & Lewis, N. K. 2019, RNAAS, 3, 7

Yip, K. H., Changeat, Q., Edwards, B., et al. 2021, AJ, 161, 4

Zechmeister, M., Reiners, A., Amado, P. J., et al. 2018, A&A, 609, A12

Zhang, J., Bi, S., Li, Y., et al. 2020, ApJS, 247, 9

Zhang, M., Chachan, Y., Kempton, E. M.-R., & Knutson, H. A. 2019, PASP, 131, 034501